



Role of Positron Emission Tomography (PET) / Computed Tomography (CT) in Evaluation of Malignant Melanoma

Essay

*Submitted for Partial Fulfillment of Master Degree in Radio
diagnosis*

By

Dr. Shaimaa AL Metwally AL Diasty AL Metwally

*M.B.,B.Ch. (2006), Resident in Radiodiagnosis Department
Faculty of Medicine, Ain Shams University*

Under The Supervision of

Prof. Dr. Khalid Talaat Khairy

*Professor of Radiodiagnosis
Faculty of Medicine – Ain Shams University*

Dr. Mohamed ElGharib Aboulmaaty

*Lecturer of Radio diagnosis
Faculty of Medicine – Ain Shams University*

*Faculty of Medicine,
Ain Shams University*

٢٠١٠

بِسْمِ اللَّهِ الرَّحْمَنِ الرَّحِيمِ

“قُلْ إِنِّي طَلَبْتُ

وَنُصِيحِي وَمَنْحِيَايَ وَمَقَاتِي

لِلَّهِ رَبِّهِ الْعَالَمِينَ (١٦٢)

لَا شَرِيكَ لَهُ وَبِذَلِكَ أُمِرْتُ

وَأَنَا أَوَّلُ الْمُسْلِمِينَ (١٦٣)”

صدق الله العظيم

الأَنْعَامُ: ١٦٢-١٦٣

List of Contents

Title	Page
• <i>Acknowledgment</i>	<i>i</i>
• <i>Abbreviations</i>	<i>ii</i>
• <i>List of Figures</i>	<i>iv</i>
• <i>List of Tables</i>	<i>ix</i>
• <i>Introduction and Aim of the Work</i>	<i>1</i>
• <i>Chapter 1:</i>	
- <i>Histopathology of Malignant Melanoma</i>	<i>3</i>
• <i>Chapter 2:</i>	
- <i>Technique of PET/CT</i>	<i>41</i>
• <i>Chapter 3:</i>	
- <i>Role of PET/CT in Malignant Melanoma with</i> <i>Illustrative Cases</i>	<i>90</i>
• <i>Summary and Conclusion</i>	<i>132</i>
• <i>References</i>	<i>133</i>
• <i>Arabic Summary</i>	<i>1</i>





ACKNOWLEDGEMENT

*First of all, thanks to **Allah** who granted me the ability to perform this work.*

*I am deeply indebted to **Prof. Dr. Khalid Talaat Khairy**, Professor of Diagnostic Radiology, Faculty of Medicine, Ain Shams University, under whose supervision this work was produced and to whom I would like to express my gratitude for his assistance and guidance throughout this work.*

*I would also like to express my grateful appreciation to **Dr. Mohammed El-Gharib Aboulmaaty**, Lecturer of Diagnostic Radiology, Faculty of Medicine, Ain Shams University, for his valuable help throughout planning and completing this work.*



Lastly I would like to thank my professors, family and all my colleagues for their continuous support and advice.

Abbreviations

AJCC	American Joint Committee on Cancer
BGO	Bismuth Germinate
CMR.....	Complete Metabolic Response
CNS.....	Central Nervous System
CT.....	Computed Tomography
DW	Diffusion weighted
FDG	Flourodeoxyglucose
FOV	Field of View
G-CSF.....	Granulocyte Colony-Stimulating Factor
GLUT	Glucose Transporter
LBG	Locust Bean Gum
LSO.....	Lutetium Oxyorthosilicate
MIS	Melanoma In Situ
MR.....	Magnetic Resonance
mSv.....	Milliseviert
NaI.....	Sodium Iodide
OCT	Optical Coherence Tomography
PET	Positron Emission Tomography
PET/CT.....	Positron Emission Tomography/Computerized Tomography
PMD.....	Progressive Metabolic Disease
PMR	Partial Metabolic Response
PMTs	Photomultiplier Tubes
SLN B	Sentinel Lymph Node Biopsy
STIR.....	Short Time Inversion Recovery
SUVmax	Maximum SUV.
US.....	Ultrasonography
UVRs	Ultraviolet Rays
WBMRI.....	Whole Body Magnetic Resonance Image

List of Figures

Fig. No.	Title	Page No.
Fig. ١,١	Primary cutaneous melanoma demonstrating irregularly shaped lesion	٧
Fig. ١,٢	Primary cutaneous melanoma demonstrating Pigmented variation	٧
Fig. ١,٣	Melanoma is situ.	١٠
Fig. ١,٤	Superficial Spreading Melanoma	١١
Fig. ١,٥	Nodular, amelanotic melanoma on the leg	١٢
Fig. ١,٦	Melanoma on the nail of the ١st toe evolving more than ٧ years	١٢
Fig. ١,٧	Lentigo Malignant Melanoma.	١٣
Fig. ١,٨	Pathway for tumor spread According to orderly progression of malignant melanoma.	١٤
Fig. ١,٩	Axial, contrast-enhanced chest CT shows multiple well-rounded soft-tissue subcutaneous nodules over the right posterior chest wall, representing metastatic melanoma.	١٥
Fig. ١,١٠	CT scan of patient with malignant melanoma of thigh revealed typical nodal involvement of right inguinal nodes.	١٦
Fig. ١,١١	Axial, contrast-enhanced CT chest in a ٣٤-year-old woman with metastatic melanoma	١٧
Fig. ١,١٢	CT scan show a military pattern of lung metastasis, multiple lung metastasis with mediastinal adenopathy and haematogenous lung metastasis with feeding vessels.	١٧
Fig. ١,١٣	CT scan of a ٥١-year old man with a history of melanoma of the back show a variety of small bowel lesions	١٩
Fig. ١,١٤	CT scan demonstrate hepatic metastasis of melanoma.	٢٠
Fig. ١,١٥A	US images shows: Abnormal gall bladder metastasis .	٢٢

Fig. 1, 10B	Photograph of the excised gallbladder shows numerous dark-brown polypoid lesions).	22
Fig. 1, 10C	Gall bladder metastasis. Axial contrast-enhanced CT image in a 29-year old woman with disseminated metastatic melanoma.	22
Fig 1, 11	CT scan of a 66 year old man with primary melanoma of the trunk demonstrate large necrotic metastasis in the spleen.	23
Fig. 1, 12	Axial non enhanced brain CT in a patient with metastatic melanoma demonstrates bilateral frontal lobe metastases..	24
Fig. 1, 13	Photograph of the gross specimen demonstrates portions of the right atrium (top) and right ventricular septum, both of which are studded with subendocardial tumorlets	25
Fig. 1, 14A	2D-parasternal long axis view. Large pericardial effusion and a well rounded mass (tumor) inside the posterior myocardial wall.	26
Fig. 1, 14B	2 cm low-density soft-tissue mass (shown with arrows) in the interventricular and interatrial septum of the heart detected on thorax CT imaging.	26
Fig. 1, 20A	multiple cystic renal metastases with mural nodules in patient with disseminated malignant melanoma	27
Fig. 1, 20B	Genitourinary tract metastasis.	27
Fig. 1, 21	Large left adrenal deposit (<i>arrowheads</i>) from metastatic melanoma.	28
Fig. 1, 22	Axial chest CT demonstrates a destructive, lytic metastasis involving the body of the T ¹¹ vertebra.	28
Fig. 1, 23	B-scan ultrasonographic appearance of choroidal melanoma with inferior retinal detachment	30
Fig. 1, 24	Pigmented conjunctival melanoma at the limbus.	31
Fig. 1, 25	Primary malignant melanoma of the Oesophagus.	32
Fig. 1, 26	Primary malignant melanoma of the rectum.	34

Fig. १,२७	Axial T ₁ weighted images MR shows hyperintense left nasal cavity mass adjacent to the intermediate intensity of inferior turbinate	३०
Fig. १,२८	T ₁ -W sagittal MR image shows a hyperintense intramedullary tumor at C _३ -C _४ level.	३६
Fig. २,१	Annihilation reaction	४४
Fig. २,२	Positron emission followed by the disintegration of a positron–electron couple.	४६
Fig. २,३	Photograph (frontal view) of a hybrid PET-CT scanner shows the PET ring detector system (red ring)	४७
Fig. २,४	Radial blurring	४८
Fig. २,०	Mean positron range and annihilation angle blurring	४९
Fig. २,६	Schematic presentation showing a ring of multiple specialized crystals detects the "coincidence" ०११-KeV photons	००
Fig. २,७	Glucose and Fluorodeoxyglucose structure	०१
Fig. २,८A	Uptake of FDG FDG is a glucose analog that is taken up by metabolically active cell	०२
Fig. २,९	A typical PET / CT scanner developed and manufactured by Gemini	०७
Fig. २,१०	PET/CT scanner shows the PET and CT component	०७
Fig. २,११	Coronal images in a ४३-year-old man after ingestion of ४ L of mannitol-LBG	६०
Fig. २,१२	Typical scout image obtained during an FDG PET/CT study	६४
Fig. २,१३	Modern PET scanners are coupled to CT scanners.	६६
Fig. २,१४	६०-year-old female patient with melanoma. (a) Axial PET and (b) fused image showing a focal (FDG) uptake in the right lower abdomen corresponding to the right ascending colon.	६७
Fig. २,१०	Photograph (side view) of a hybrid PET-CT scanner shows the PET (P) and CT (C) components	६८

Fig. ٢,١٦	Whole-body FDG acquisition protocol for the prototype PET/CT	٦٩
Fig. ٢,١٧	Typical imaging protocol for combined PET/CT	٧٠
Fig. ٢,١٨	PET/CT image consisting of coronal whole-body CT image PET image with CT attenuation correction.	٧١
Fig. ٢,١٩	Normal distribution of FDG physiologic accumulation of FDG in the cerebral-cerebellar cortex at the base of the skull and in the myocardium, liver, kidneys.	٧٣
Fig. ٢,٢٠	Coronal FDG PET scan (a) and transverse fused PET/CT image obtained at the level of the stomach.	٧٤
Fig. ٢,٢١	Heterogeneous physiologic bowel uptake	٧٤
Fig. ٢,٢٢	Physiologic testicular uptake in a ١٦-year-old boy with a history of lymphoma of the left tibia.	٧٥
Fig. ٢,٢٣	Benign ovarian ١٨F FDG uptake in a ١٥-year-old girl with a history of large B-cell lymphoma in the abdomen	٧٦
Fig. ٢,٢٤	Symmetric uptake in normal tonsils (arrows) as well as bilateral mild uptake in the parotid glands.	٧٦
Fig. ٢,٢٥	Increased uptake in the diaphragm and intercostals muscles	٧٧
Fig. ٢,٢٦	Curvilinear cold artifact (arrow) is commonly seen on dome of diaphragm/liver or at lung base because of respiration mismatch on PET images with CT attenuation correction	٦٥
Fig. ٢,٢٧	٥٨-y-old man with colon cancer. Lesion at dome of liver is mislocalized to right lung (arrow) because of respiratory motion	٨٤
Fig. ٢,٢٨	Attenuation correction artifact	٨٦
Fig. ٢,٢٩	High-density metal artifacts	٨٦
Fig. ٢,٣٠	٦١-y-old patient with lung cancer who ingested barium for an esophagogram ١ d before PET/CT scan	٨٧
Fig. ٢,٣١	CT scan shows intravenous contrast medium	٨٨

	in right subclavian vein (arrow	
Fig. ٢,٣٢	٥٤-y-old man with history of metastatic melanoma (arrow). CT image appears truncated at sides	٨٩
Fig. ٣,١	A ٥٩-year-old male after resection of a malignant melanoma of the left dorsal thorax (initial clinical stage II	٩٥
Fig. ٣,٢	Intense hyper metabolic right axillary focal activity, compatible with malignant melanoma.	٩٥
Fig. ٣,٣	Transaxial PET, CT, and fused PET/CT images demonstrate widespread metastases in the brain (white arrowheads), lung (black arrowheads), subcutaneous soft tissue (black arrows), and peritoneum (white arrows)	٩٧
Fig. ٣,٤	Transaxial PET, CT, and fused PET/CT images show thyroid (white arrowheads), pulmonary (black arrowheads), and left adrenal (arrows) metastases	٩٨
Fig. ٣,٥	Transaxial PET, CT, and fused PET/CT images Liver metastases (arrowheads) are noted	٩٩
Fig. ٣,٦	Metastasizing melanoma in a young lactating woman	١٠٠
Fig. ٣,٧	Transaxial PET image shows irregular intense ^{١٨} F-FDG uptake in mid-thoracic spine (B) Corresponding CT image shows increased Para vertebral soft tissue (C) PET/CT fusion images demonstrate metastasis in right Para vertebral region with extension through neural foramen into spinal canal.	١٠٢
Fig. ٣,٨A	Transaxial slice of the co-registered F-١٨ FDG PET/CT image of the whole body F-١٨ FDG PET/CT scan. The fusion image unequivocally reveals the F-١٨ FDG avid character of the lesion, which, in view of the	١٠٣

	patient's history, is highly suspicious to be a metastasis from a cutaneous melanoma, and cholecystectomy was done	
Fig. ٣, ٨B	Focal uptake in right upper quadrant (A, Transaxial PET image). (B) This was shown in PET/CT fusion image (lower panel) to be in gallbladder, later confirmed by sonogram and CT.	١٠٣
Fig. ٣, ٩	Axial PET-CT images for restaging (upper images: solely CT revealed a midabdominal intussusception.	١٠٥
Fig ٣, ١٠	Axial PET-CT images: There are multiple soft tissue FDG avid lesions in the abdomen involving the bowel/mesentery (left flank, mid lower abdomen), porta hepatis region, the right lower quadrant subcutaneous tissue and the right adrenal gland.	١٠٦
Fig. ٣, ١١A	PET (left) axial CT (upper right) axial PET/CT (lower right) showing multiple focal abnormal areas of increased FDG uptake of an intense nature involving the soft tissues posterior and closely adjacent to the proximal right humerus.	٨٤
Fig. ٣, ١١B	Focal abnormal area of increased FDG uptake of an intense nature involving soft tissues of the lower left buttock adjacent to the muscle (red and grey arrow	١٠٧
Fig. ٣, ١٢A	Transverse fused PET/CT image shows two pulmonary nodules (arrows) in lower lobes (b) Corresponding transverse PET image and (c) coronal maximum intensity projection show no FDG uptake.	١٠٨
Fig. ٣, ١٢B	PET/CT image shows progression of pulmonary nodules (arrows) in size and number (e) Corresponding transverse PET image and (f) coronal maximum intensity projection show increased FDG uptake in several lung nodules (arrows)	١٠٩
Fig. ٣, ١٣	FDG PET maximal intensity projection image shows focal, intense tracer uptake in	١٠٩

	the mid-right thigh (yellow arrow) (b) Axial FDG PET and (c) PET/CT fusion images of the lower extremities showing intense, focal FDG uptake localizing to the mid shaft of the right femur (red crosshairs) suggestive of metastatic disease	
Fig. ३, १६	Maximum intensity projection (MIP) image (B, C and D) Transaxial PET/CT images show widespread metastatic disease including three ST lesions in the left scalp (arrow), left mid back (arrow head) and left distal thigh (pentagon).	११०
Fig. ३, १०	The images show an intense gut-associated focus in the left abdomen (arrows), strongly suspicious of recurrence. However, a structural lesion that could be biopsied was evident only १ months later.	१११
Fig. ३, १६	Complete metabolic response	११६
Fig. ३, ११	Maximum image projection (MIP) image at baseline demonstrates nodal disease in the left axilla and anterior mediastinum, bony metastasis in right ०th rib and sacrum	११६
Fig. ३, ११	PET/CT re-staging after three cycles chemotherapy (lower panel) demonstrates progressive disease with more extensive disease in the left axilla and new metastasis in a subcentimetre supraclavicular node	११०
Fig. ३, ११	Transverse fused PET/CT image shows small lesion (arrow) in gluteal subcutaneous fatty tissue on right side (B) Corresponding transverse PET	१११
Fig. ३, १०	corresponding PET/CT image, the same lymph node is seen as FDG avid and was thus evaluated as metastasis	१११
Fig. ३, ११	Axial (A) CT, (B) attenuation corrected PET, and (C) fused PET/CT images demonstrate diffuse metastatic disease within the mediastinum along with innumerable pulmonary metastases	११०
Fig. ३, ११	AeB: axial १D T१-weighted MR slices. CeD:	१११

	corresponding axial YD attenuation-corrected PET images. Two lesions with spontaneous hyperintensity are visible in hepatic segments I and VIII (yellow arrows)	
Fig. ३,२३	Axial FDG PET and (b) PET/CT fusion images of the brain showing focal hypometabolism in the right frontal cortex with a subtle rim of increased FDG uptake noted along the posterolateral border	१२३
Fig. ३,२४	The left axillary lymph node is well visualized by both MRI and PET-CT (orange arrows). Its size is around १0mm . On the contrary, small bilateral iliac lymph nodes, whose size is $0\text{ } १\text{mm}$, are only displayed on DWI sequence (black arrows)	१२६
Fig. ३,२०	PET/CT (A–D) and wbMRI (E–H) of a ३१-year-old male with metastatic melanoma. CT and MRI found more lung metastases than PET (B/F, arrowheads) and MRI found more liver lesions than PET/CT	१२१
Fig. ३,२६	Case of two secondary hepatic metastases (segments V and VI) clearly observed on a DWsequence (on the left). The lesion located in the segment V is not seen by PET-CT (on the right) because of a moderate physiological hyper-metabolism	१२४
Fig. ३,२१	CT from PET/CT (A) demonstrates subtle lesions having increased attenuation, compatible with hemorrhagic brain metastases.	१२१
Fig. ३,२४	२१ years old man. Examples of secondary distant bone metastases only visible on the MRI examination. These metastases are clearly seen as abnormal hyper-signal areas on the STIR sequence	१३०
Fig. ३,२१	fused PET/CT image (b) show a solitary bone lesion in a thoracic vertebral body (arrow). MRI (sagittal contrast-enhanced fat saturated image, c) shows multiple disseminated enhancing bone metastases	१३०

List of Tables

<i>Table. No.</i>	Title	Page No.
<i>Table 1.1</i>	Clark's Classification.	۳۷
<i>Table 1.2</i>	Prognostic indicator of melanom	۳۸
<i>Table 1.3</i>	Revised Melanoma Staging..	۴۰
<i>Table 2.1</i>	Radionuclides used in PET	۵۵
<i>Table 2.2</i>	Average adult PET and PET/CT scan times.	۶۸

Introduction and aim of work

Introduction:

The incidence of melanoma is increasing more rapidly than any other malignancy (*Rigel and Carucci, 2000*) Melanoma currently ranks as the fifth most common cancer, with an estimated 62190 cases diagnosed in 2006 (*Jemal A et al., 2006*), Although melanoma most commonly metastasizes to regional lymph nodes, mortality from melanoma is due primarily to distant spread to visceral organs, commonly the lung, liver and brain (*Blach et al., 2001*), Long – term survival is excellent for patients diagnosed with in situ and early invasive disease, making an early diagnosis and accurate staging extremely important in the management of melanoma (*Lange and Blach, 2006*).

For many years, computed tomography (CT), and to a lesser extent magnetic resonance imaging (MRI), have been the principal modalities used for imaging metastatic melanoma, however, the advent of positron emission tomography (PET), and more recently PET/CT, has raised new questions as to be the optimal imaging management strategy for the this disease, as they combine the ability to detect active metabolic processes and their morphologic features in a single exam, so it play important role in staging and restaging of malignant melanoma (*Gambhir , 2002*).

FDG-PET is of limited use in patients with early-stage disease without nodal or distant metastases (stage I-II), but FDG-